Article
Journal of
Nanoscience and Nanotechnology
Vol. 17, 1–10, 2017
www.aspbs.com/jnn

Versatile Fe-Containing Hydroxyapatite Nanomaterials as Efficient Substrates for Lead Ions Adsorption

D. F. Mercado[1], A. Rubert[1], G. Magnacca[2], M. Malandrino[3], S. Sapino[4], P. Caregnato[1],
A. Bianco Prevot[5], and M. C. Gonzalez[1,*]

[1] Instituto de Investigaciones Fisicoquímicas Teóricas y Aplicadas (INIFTA), CCT-La Plata-CONICET,
Facultad de Ciencias Exactas, Universidad Nacional de La Plata, C.C. 16, Su.4, La Plata, Argentina
[2] Dipartimento di Chimica, NIS and INSTM Reference Centre, Università di Torino, via Giuria 7, Torino, Italy
[3] Dipartimento di Chimica, and NIS Centre, Università di Torino, via Giuria 7, Torino, Italy
[4] Dipartimento di Scienza e Tecnologia del Farmaco, Università di Torino, via P.Giuria 9, Torino, Italy
[5] Dipartimento di Chimica, Università di Torino, via Giuria 7, Torino, Italy

The capability of paramegnetic iron-containing hydroxyapatite (Fe-nAp) and waste bioorganic subtrates templeted iron-containing hydroxyapatite (SBO-Fe-nAp) nanoparticles, as Pb(II) cations adsorbants were investigated and compared to those of synthetic hydroxyapatite (nAp). Surface and bulk characterization techniques as XPS, XRD, electrophoretic mobility, FTIR spectroscopy, DLS, and TEM were used to investigate the adsorption mechanisms involved and ICP-AES to determine Pb(II) concentrations in aqueous solutions. The apatite-based nanoparticles were found to be efficient materials for the irreversible adsorption of Pb(II) ions from aqueous solutions, with maximum adsorption capacity increasing as: hydroxyapatite $<$ waste bioorganic subtrates templeted iron-containing hydroxyapatite $<$ iron-containing hydroxyapatite. Adsorption capacities of 1500 mg g^{-1} observed for iron-containing hydroxyapatite, are among the highest reported for Pb(II) adsorption. The high surface to volume ratio, low crystallinity, and the negatively charged surface, strongly favour aqueous Pb(II) adsorption on Fe-containing apatites over the positively charged crystalline hydroxyapatite. The adsorption mechanisms involved depend on the available surface hydroxyl and carboxyl groups as well as on the formation of stable lead-containing hydroxyapatite-like structures. Moreover, bimetal adsorption experiments involving Cu(II) and Pb(II) ions show particular selectivity depending on the surface chemistry of the hydroxyapatite-based adsorbent. While hydroxyapatite is selective towards Pb(II), Fe-containing hydroxyapatite selectivity depends on the relative [Pb]/[Cu] ratio, and waste bioorganic subtrates templeted Fe-containing hydroxyapatite, adsorbs both ions with similar capability.

Keywords: Paramagnetic Nanoparticles, Pb(II) Adsorption, Cu(II) Adsorption, Bio-Organic Substrates, Surface Chemistry.

1. INTRODUCTION

Contamination by traces of Pb(II) ions represents one of the most pressing and potentially costly threats to water and soil resources as well as a serious threat to human health. Published studies demonstrated that apatite may stabilize *in situ* Pb(II) species present in contaminated soil reducing the Pb bioavailability.[1–3] Hydroxyapatites of different origins, denoted herein as Ap, as synthetic nanohydroxyapatite (nAp),[1,3] eggshell waste,[4] cow bone powder,[5] etc. were used as efficient lead ions adsorbents. Literature reports suggest that Ap removes Pb(II) via dissolution followed by hydroxypyromorphite precipitation ($Pb_5(PO_4)_3X$ with X: OH, F, or Cl) with Pb(II) removal efficiency of 37 to 100%. Pyromorphite has been suggested as the end of a process in which $Pb_{(10-x)}Ca_x(PO_4)_6(OH)_2$ crystallites are firstly formed and then dissolved to precipitate crystals with lower calcium content.[1] Dissolution of pyromorphite is favoured by phosphate-deficient environments. Metal ions such as Al(III), Cu(II), Fe(II), Cd(II), Zn(II), and Ni(II) inhibit Pb(II) immobilization by hydroxyapatite

---

[*] Author to whom correspondence should be addressed.

1533-4880/2017/17/001/010 doi:10.1166/jnn.2017.13870

because the precipitation of amorphous to poorly crystalline metal phosphates decreases the amount of dissolved phosphate available.[6]

Since pyromorphite is in equilibrium with aqueous Pb(II)[7] with concentrations of the order of EPA drinking water limits (15 μg L^{-1}), Pb(II) immobilization as pyromorphyte reflects in a reduced availability to many living systems. Due to hydroxyapatite and pyromorphite long stability in the environment, Ap materials have gained considerable attention as Pb(II) sequestration agents for remediation of contaminated soil and wastes.[8]

Several studies pointed to the solid–liquid interface of apatite materials and phosphate rocks as responsible for the materials particular affinity for metal ions capture and also for the capture mechanism.[7, 9–11] For instance, formation of insoluble fluoropyromorphite was primarily responsible for Pb immobilization on phosphate rocks with less significant contribution from surface adsorption and/or complexation, whereas the reversed situation was observed for Cu(II) and Zn(II).[12]

The maximum adsorption capacities (b) towards Pb(II) ions reported for apatites of different morphology, size, and surface chemistry, are shown in Table I. An analysis of this data seems to suggest that apatite materials show more efficient Pb(II) adsorption properties when they are either poorly crystalline, nanomatric, and combined with magnetite nanoparticles.

Synthetic paramagnetic iron-containing hydroxyapatite nanoparticles (Fe-nAp) and soluble bio-organic substrates-templated Fe-nAp, denoted as SBO-Fe-nAp were previously synthetized in our group.[10] These materials combine nanometric size, loss of crystallinity, a higher specific surface area, and formation of surface iron phases. In the present work we investigate the Pb(II) adsorption capacity and mechanisms of the iron-containing hydroxyapatite nanoparticles of different surface chemistry, Fe-nAp and SBO-Fe-nAp, and on iron-free hydroxyapatite, nAp, in an attempt to find new nanomaterials with an improved capacity for Pb(II) adsorption. Moreover, Pb(II) affinity was compared to that of Cu(II) in bimetal competitive adsorption experiments.

Table I. Maximum adsorption capacity (b) given as mg g^{-1} reported for different hydroxyapatites as adsorbents of Cu(II) and Pb(II) ions. Solution pH is in the range 6–7.

Particle type	b Cu(II) (mg g^{-1})	b Pb(II) (mg g^{-1})
Swine Bone Ap		64.1[4]
Synthetic Ap	23.7 [13]	91.6 [14]
Gypsum waste poor Crystalline Ap		500 [15]
Carbonate Ap		101 [4]
Nano Ap	50 [10] 65–87 [3]	79–92 [3] 357 [16]
Fe-containing nano Ap	265 [10]	
Nano Ap/Fe$_3$O$_4$		599 [17]

2. EXPERIMENTAL DETAILS

2.1. Reactants

Lead nitrate (≥99.99% trace metals basis) was supplied by Sigma Aldrich and used without further purification. Deionized water was Milli-Q purified (18.2 MΩcm and 6 ppb TOC). The pH in the adsorption experiments was stabilized to 7.0 with 4-(2-hydroxyethyl)piperazine-1-ethanesulfonic acid, sodium salt (HEPES-Na) and nitric acid, while acetate buffers were used to adjust the pH in the desorption experiments.

The different nanoparticles, hydroxyapatite (nAp), iron-containing hydroxyapatite (Fe-nAp), bio-organic substrates-templated iron-containing hydroxyapatite (SBO-Fe-nAp), and calcinated at 600 °C SBO-Fe-nAp (SBO-Fe-nAp-cal), respectively, were obtained as described previously in the literature.[10]

2.2. Metal Adsorption Experiments

Adsorption studies were conducted in batch experiments. Variable ml-aliquots of a Pb(NO$_3$)$_2$ stock solution of 1000.0 mg L^{-1} were mixed with 5 ml of a 100 ppm solution of either nAp, Fe-nAp, SBO-Fe-nAp, or SBO-Fe-nAp-cal, and further diluted to a final volume of 25 mL with a solution of 4-(2-hydroxyethyl)piperazine-1-ethanesulfonic acid sodium salt (HEPES-Na) of pH 7 and 0.01 M ionic strength. Under such experimental conditions, HEPES does not form complexes with the metal aqueous ions.[13]

The suspensions were vigorously shaken at room temperature (25 ± 2 °C) for several hours until equilibration was observed. To that purpose, the supernatant and solid residues were separated by centrifugation at 4,000 rpm for 10 min and the Pb(II) concentration in the supernatant solution determined by ICP-AES. Preliminary experiments done analyzing the solution concentration of Pb(II) after 30 minutes, 3 and 24 hours showed that Pb(II) solution concentration remains constant after 3 hours of mixing, thus indicating that equilibration takes place already at that period of time. The amount of adsorbed Pb(II) was calculated according to $x/m = v \times (C_o - C_e)/m$, where x/m (mg g^{-1}) is the weight in mg of Pb(II) ions adsorbed per g of particles; C_o and C_e (mgL^{-1}) stand for Pb(II) concentration in the starting solution and after adsorption and equilibration, respectively; v(L) is the solution volume used in the experiment and m(g) is the mass of particles used. Data were expressed as the mean of three replicates.

In bimetal experiments, increasing concentrations of Pb(II) were added to a suspension of the particles already containing 6.4 ppm Cu(II) maintaining the experimental conditions of pH, ionic strength and particle concentration used in one metal experiments. After three hours mixing to reach equilibration, both, Pb(II) and Cu(II) concentrations in the aqueous solutions were simultaneously determined by ICP-AES.

Metal determinations were performed with a Perkin Elmer Optima 7000 DV Model inductively coupled plasma atomic emission spectrometer (ICP-AES). The instrument is equipped with a Echelle monochromator, a cyclonic spray chamber, and a PTFE Mira Mist nebulizer. The instrumental conditions were: plasma power 1.3 kW; sample aspiration rate 1.2 mL/min; argon cooling flow 15 L/min; argon sampling flow 0.6 L/min. The lower limit sensitivity for Pb(II) quantitative determination by the ICP-AES method used is on the order of 20 ppb.

2.3. Particle Characterization

Nanoparticles containing adsorbed Pb(II) were further characterized to gain information on size, crystalline domains, surface composition, surface chemistry, surface charge, and aggregation in aqueous suspensions.

X-ray Diffraction (XRD) experiments were performed with a PW3040/60 X'Pert PRO MPD X-ray diffractometer from PANalytical, in Bragg-Brentano geometry, equipped with the high power ceramic tube PW3373/10 LFF source with Cu anode.

Transmission Electron Microscopy (TEM) micrographs were obtained with a JEOL 1200 EX II instrument. Samples were dry deposited on carbon-coated copper grids.

The functional groups present in the prepared nanoparticles were identified by their IR spectrum obtained with a Bruker IFS28 spectrophotometer equipped with a Globar source and a DTGS detector working at 128 scans with 4 cm^{-1} resolution in the overall range 4000–400 cm^{-1}.

The X-ray Photo-electron Spectroscopy (XPS) spectra were obtained under UHV with a XR50 Specs GmbH spectrometer using Al K(α) as the excitation source and a PHOIBOS 100 half sphere electron energy analyzer. A two-point calibration of the energy scale was performed using sputtered cleaned gold (Au $4f7/2$ binding energy (BE) of 84.00 eV) and copper (Cu $2p3/2$, BE: 932.67 eV) samples. Internal calibration to correct for surface charging was performed with the C1s peak at BE = 284.6 eV due to adventitious carbon. High resolution XPS spectra were taken to get a better insight into the chemical environment of the different atoms. A Shirley-type background from each spectrum was used to remove the effect of the extrinsic structure loss and the espectrum resolved by Gaussian-Lorentzian fitting, keeping $\chi 2$ values to their minimum values. The outer shell chemical composition of the particles was estimated considering the experimental sensitivity factors of the different elements.

Dynamic Light Scattering (DLS) and electrophoretic mobility experiments were obtained at 25 ± 0.1 °C with a 90 Plus Particle Size Analyzer (Brookhaven Instrument Corporation, Holtsville, NY, USA) at a fixed angle of 90° after appropriate dilutions. Each system was analyzed three times.

3. RESULTS AND DISCUSSION

The particles composition, size, aggregation, and surface chemistry were thorougly determined and described in a previous publication.[10] Scheme 1 summarizes the particular characteristics of the hydroxyapatite-based particles used as sorbents for the uptake of lead from aqueous solutions. Also, the adsorption capacity of calcinated SBO-Fe-nAp (denoted as SBO-Fe-nAp-cal) was determined for comparison purposes. However, since SBO-Fe-nAp-cal shows similar surface properties and chemistry than nAp-Fe, it is not shown in Scheme 1.

3.1. Metal Adsorption Capacity

Figure 1 shows Pb(II) adsorption isotherms for the different particles obtained following the protocol already described. The one-adsorption site Langmuir model, Eq. (1), fits all the isotherms with regression coefficients $r^2 > 0.95$. The fitting parameters obtained are reported in Table II. The maximum number of sites b increases in the order nAp < SBO-Fe-nAp < Fe-nAp ≅ SBO-Fe-nAp-cal while the affinity coefficient of Pb(II) adsorption, K_L, shows the following trend: nAp < Fe-nAp ≅ SBO-Fe-nAp-cal < SBO-Fe-nAp.

$$\frac{x}{m} = \frac{K_L \times b \times C_e}{1 + K_L \times C_e} \tag{1}$$

Values of b (in mg g^{-1}) observed for nAp are of the same order of those reported for synthetic nanohydroxyapatite[3, 14] in the pH range 6.25–7.0, but between 4 to 10 times higher than those reported for phosphatic clay[15] and cow bone apatites.[5] On the other hand, K_L values obtained are of the same order of those reported for apatites of different origin.[2, 4, 15, 16]

Fe-nAp shows b values almost ten times higher than those calculated for nAp. On one side, literature reports indicate that Fe(II) inhibits Pb(II) immobilization by hydroxyapatite due to the formation of amorphous iron phosphates leading to a decreased amount of dissolved PO_4^{3-} available for Pb(II) precipitation.[17] On the other side, the maximum adsorption of Pb(II) on pure magnetite materials were reported to be in the range between 91 and 20 mg g^{-1} [18, 19] whereas hydroxyapatite/Fe_3O_4 composites showed maximum adsorption capacities of 599 mg g^{-1},[20] in line with the high values observed here.

SBO-Fe-nAp isotherms show lower b values than Fe-nAp, thus suggesting that SBO components adsorbed to the particles surface (as illustrated in Scheme 1) partially shields the surface behaviours assessed by the Fe-nAp core. In fact, calcinated SBO-Fe-nAp, not containing adsorbed organic carbon,[10] shows a Pb(II) ions adsorption isotherm coincident with that of Fe-nAp (see Fig. 1). The similar adsorption properies SBO-Fe-nAp-cal and Fe-nAp are further supported by their almost identical surface and crystalline properties.[10]

To investigate the effect of the surface area on the adsorption efficiency of the particles, isotherms were normalized to the specific surface areas of 34, 64, 71 and

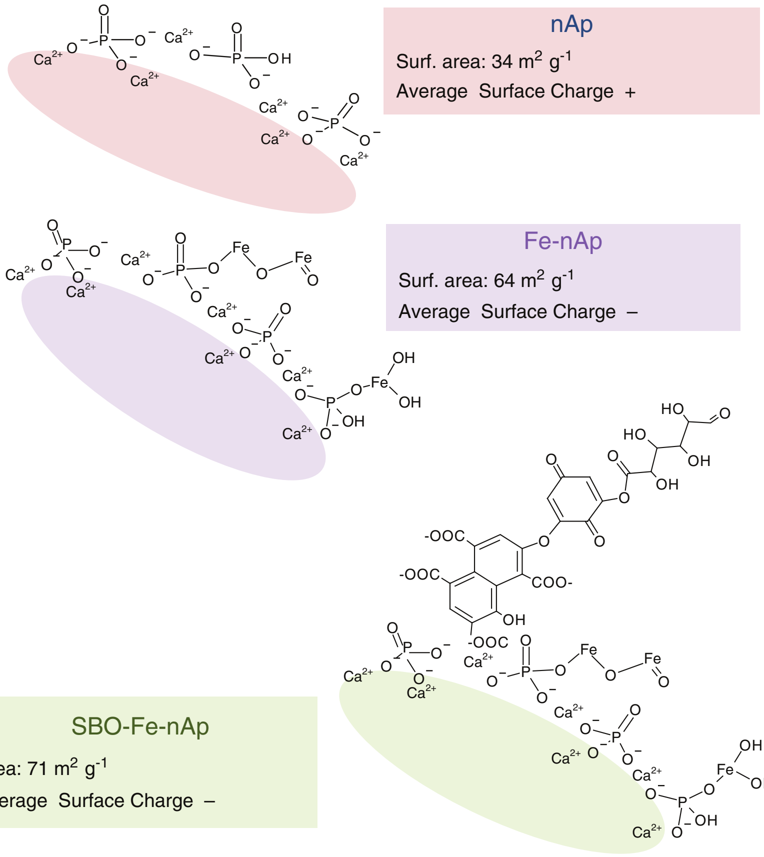

Scheme 1. Illustrative surface representation of the different particles used as sorbents.

64 m^2 g^{-1} of nAp, Fe-nAp, SBO-Fe-nAp, and SBO-Fe-nAp-cal, respectively, as determined by N_2 adsorption and BET model analysis. The normalized isotherms are shown in Figure 1 *inset*, and the maximum Pb(II) surface loading expressed as moles of ions per unit area, Γ, are reported in Table II. Fe-nAp and SBO-Fe-nAp show similar uptake efficiency at low particle coverage, but Fe-nAp shows higher capacity of capturing Pb(II) ions than SBO-Fe-nAp at high surface coverage. On the other hand, the lower Γ observed for nAp with respect to Fe-nAp and SBO-Fe-nAp is clearly not related to the smaller surface to volume ratio of nAp, but to particular surface characteristics enhancing Pb(II) adsorption upon iron incorporation.

To determine the release of Pb(II) from the treated substrates, approximately 0.5 mg of nAp, Fe-nAp, and SBO-Fe-nAp powders equilibrated with $C_e \approx 4$ mgL^{-1} of Pb(II) solutions were filtered. The obtained filtrates were further re-suspended in 25 ml of aqueous solutions of $4.5 < pH < 7.5$. After twenty four hours, all the materials showed

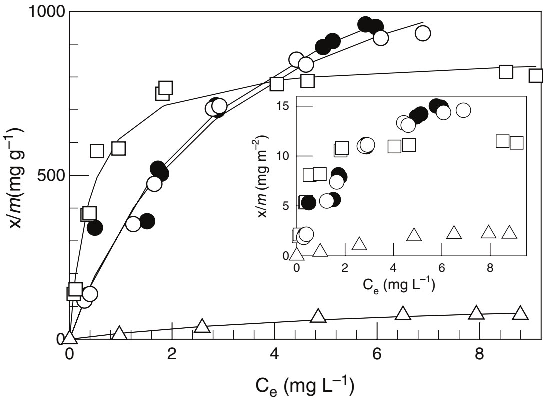

Figure 1. Pb(II) ions adsorption isotherms at 25 °C and 20 mg/L of Fe-nAp (●), SBO-Fe-nAp-cal (○), SBO-Fe-nAp (□), and nAp (Δ). The solid lines stand for the fitting of the data according to Eq. (1). *Inset*: Isotherms normalized to the specific surface area of the materials.

Table II. Fitting parameters calculated according to equation (1) and maximum surface loading, Γ. Error bars are denoted in parentheses.

Particle	b/mg g^{-1}	K_L	r^2	Γ/μmol m^{-2}
nAp	140 (30)	0.15 (0.07)	0.978	20
e-nAp	1500 (150)	0.30 (0.07)	0.984	113
SBO-Fe-nAp	870 (25)	2.4 (0.3)	0.994	59
SBO-Fe-nAp-cal	1400 (70)	0.32 (0.07)	0.994	106

$<$20 ppb Pb(II) leaching, indicating an irreversible Pb(II) adsorption in the studied pH range.

3.2. Pb(II)-Sorbed Particles Characterization

Information on the involved adsorption processes could be obtained from the thorough characterization of filtered nAp, Fe-nAp, and SBO-Fe-nAp powders after equilibration with $C_e \approx 4$ mgL^{-1} of Pb(II) solutions. The obtained powders will be denoted as: Pb//nAp, Pb//Fe-nAp, and Pb//SBO-Fe-nAp. No further characterization studies were performed with Pb(II)-adsorbed SBO-Fe-nAp-cal because the physicochemical and adsorption properties of SBO-Fe-nAp-cal showed no differences with those of Fe-nAp. It should be noted that the samples submitted to physicochemical characterization were obtained from adsorption experiments using larger volumes of materials and therefore may not exactly reproduce the favorable mixing conditions under which the adsorption isotherms were obtained.[21]

TEM images of Pb//nAp, Pb//Fe-nAp, and Pb//SBO-Fe-nAp were compared with those of Pb(II)-free particles. Figure 2 shows Pb//nAp and Pb//Fe-nAp TEM micrographs. Due to substantial agglomeration it is not possible to obtain a statistic analysis of the particles size. Pb//nAp particles mantain nAp rod-like morphology of *c.a.* 70–150 nm length, varying thickness, and smooth borders. Pb//Fe-nAp and Pb//SBO-Fe-nAp particles show 50–100 nm size and a cicular shapes with irregular edges already observed for the respective Pb(II)-free particles and attributed to the effect of Fe ions incorporation.[10] These observations indicate that Pb(II) adsorption does not significantly affect the morphology of the particles.

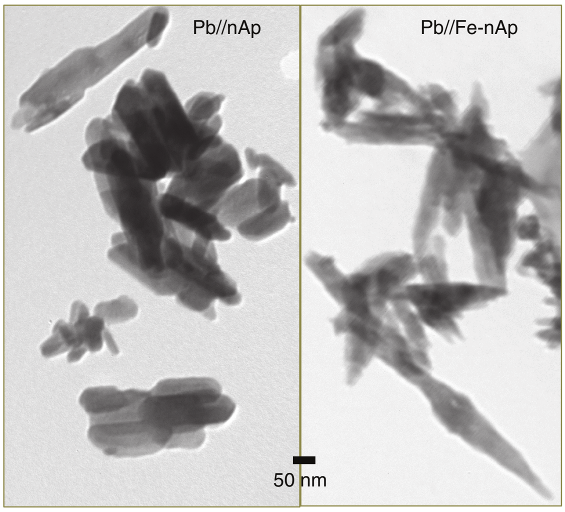

Figure 2. TEM micrographs of Pb//nAp and Pb//Fe-nAp.

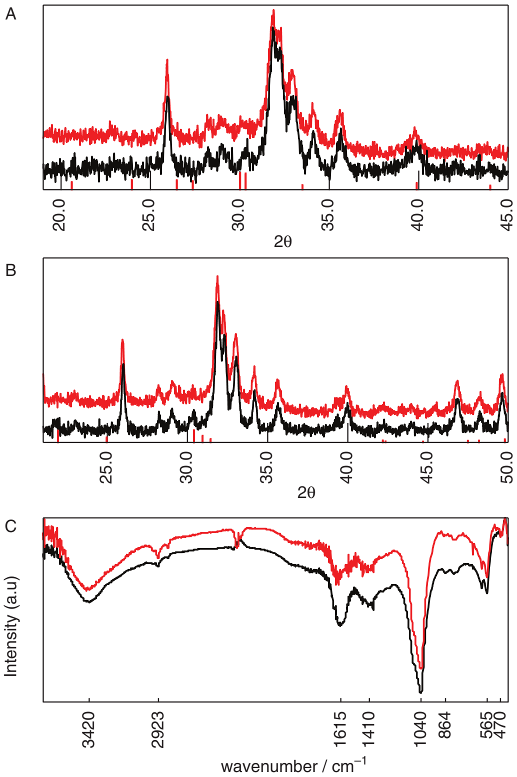

Figure 3. (A) X-ray diffractograms of Fe-nAp and Pb//Fe-nAp, from top to down respectively. Bars stand for $Ca_2Pb_3(PO_4)_3Cl$ principal reference patterns. (B) X-ray diffractograms of SBO-Fe-nAp and Pb//SBO-Fe-nAp, from top to bottom respectively. Bars stand for pyromorphite principal reference patterns. (C) FTIR spectra from top to down: SBO-Fe-nAp and Pb//SBO-Fe-nAp, respectively.

Corresponding XRD diffractograms of Pb//nAp, Pb//Fe-nAp, and Pb//SBO-Fe-nAp (see Figs. 3(a and b) for the diffractograms of the last two powders) showed hydroxyapatite patterns and peak widths very similar to those of nAp, Fe-nAp, and SBO-Fe-nAp, respectively. Thus suggesting that the particles hydroxyapatite crystalline domain is not significantly modified by Pb(II) adsorption.[1] Of much less significance, the diffractogram of Pb//Fe-nAp also shows two diffraction peaks at $2\theta =$ 22 and 30 which could be assigned to the presence of a phosphohedyphane-like structure ($Ca_2Pb_3(PO_4)_3Cl$) whose principal peaks of the diffraction pattern are depicted in Figure 3(a).[22] On the other hand, the small diffraction peaks at 2θ *ca.* 30.0, 23.9, and 17.8 observed for Pb//SBO-Fe-nAp are in coincidence with those of pyromorphite, see Figure 3(b), and are therefore assigned to this species.

The FTIR spectrum of Pb//SBO-Fe-nAp (see Figs. 3(c)) shows the fundamental vibration modes of PO_4^{3-} groups of the apatitic structure at about 470, 560, 610, and 1030–1100 cm^{-1}.[23] The intense bands at 3430 and 1649 cm^{-1} indicates the presence of HO groups of phenols, alcohols and carboxyl groups, and of C=O bonds of carboxyl and carbonyl moieties, respectively, already observed for SBO-Fe-nAp and attributed to SBO components physisorbed to the particles surface, as illustrated in Scheme 1. The absorption bands at 1600 and 1410–1380 cm^{-1}, which are markedly enhanced compared to those of SBO-Fe-nAp (also shown in Fig. 3(a)), may be assigned to the formation of complexes between $Pb^{2+}/Pb(OH)^+$ and SBO carboxyl groups, as those formed in the presence of phenolic and carboxylic groups of humic acids in the pH range from 4 to 9.[24–26] In fact, metal carboxylates show strong absorption bands in the 1550–1620 cm^{-1} and weaker ones around 1410 cm^{-1} region. Those bands are assigned to asymmetric and symmetric COO^- group stretching modes and their separation of $\Delta\nu \sim 200$ cm^{-1} is compatible with bidentate metal-carboxylate bridging modes.[27]

The XPS survey spectra of Pb//nAp, Pb//Fe-nAp, and Pb//SBO-Fe-nAp materials show the main lines of Ca, O, P, Fe (except for nAp), and Pb, as depicted in Figure 4 top graph. Beside these peaks, a C1*s* "adventitious carbon" peak was asigned (roughly involving all the rest of low binding energy carbon species) and used for binding energy correction due to charging effects by setting it to 284.6 eV. All the materials show the contribution of a C1*s* peak at 288.5 eV attributed to carboxylic acids, metal carbonates, and Pb-carboxyl complexes.[28] The contribution of the latter peak, together with a component at 285.5 eV attributed to organic ethers and esters, is especially important for Pb//SBO-Fe-nAp, whose signals are reported in Figure 4, bottom graphs.

All powders show Ca2*p*1/2 and Ca2*p*3/2 lines at 347.4 eV separated by 3.5 eV, and P2*p*1/2 and P2*p*3/2 lines at 133 eV separated by 0.9 eV, as expected for the apatite moieties. Fe2$p3/2$ and Fe2$p1/2$ signals for Pb//Fe-nAp and Pb//SBO-Fe-nAp were modelled using a combination of ferrous and ferric multiplet patterns for the lower and higher energy portion of the spectrum, respectively.[10] Both Pb//Fe-nAp and Pb//SBO-Fe-nAp samples show Fe2$p3/2$ contributing peaks at 710.9, 712.2, 713.4, and 714.9 eV, as well as the presence of Fe^{2+} satellite peak shifted by 4.8–5 eV, in line with the patterns reported for Fe-nAp and SBO-Fe-nAp. These observations strongly suggest that Pb(II) adsorption shows no significant effect on Fe(II)/Fe(III) phosphates and oxides, in line with literature reports on Pb(II) adsorption on geothite.[29]

O1*s* peaks show the main contribution of bands at 530.1 and 532 eV, and an additional band at 530.1 eV which is only observed for Fe-containing particles. These peaks are assigned to oxygen atoms in phosphate and hydroxyl groups, to adsorbed water and/or organic oxygen, and to iron oxide environments, respectively. Additionally, Pb4$f5/2$ and Pb4$f7/2$ peaks ($\Delta BE = 4.87$ eV) show a main contribution peak at 138.9 eV, typical of Pb(II) inorganic salts and lead carboxylates.[28, 30] Interestingly, no significant contribution arround 137 eV due to lead oxides are observed.

XPS sampling extends to depths of a few nanometers depending on the emitted electron energies and density of the upper layers. Therefore, this technique yields information on the 1–4 nm depth outer shell of the particle volume.[31] The outer shell chemical composition of the particles obtained from the XPS experiments is depicted in Table III. Pb//Fe-nAp shows *ca*. 10% lower Ca:P ratios than the corresponding Pb(II)-free particles probably indicating an exchange of Ca(II) by Pb(II) ions. On the other hand, the presence of adsorbed Pb(II) does not modify, within the experimental error, Ca:P:O surface ratios of SBO-Fe-nAp, while the oxygen content is increased by the incorporation of Pb(II) in nAp.

The electrophoretic mobilities of Pb//Fe-nAp and Pb//SBO-Fe-nAp are less negative than those of their corresponding Fe-nAp and SBO-Fe-nAp precursors, while that of Pb//nAp is, within the experimental error, similar to that of nAp, as shown in Table III. Since the electrophoretic experiments were performed under identical conditions of ionic strength and temperature and considering that the size and shape of the particles is not significantly alterated by Pb(II) adsorption (*vide supra*), differences in the mobility of Pb(II)-sorbed and Pb(II)-free particles mainly depend on differences in the particles surface charge.

Pb//nAp, Pb//Fe-nAp, and Pb//SBO-Fe-nAp hydrodynamic sizes in aqueous suspensions at pH 7 and 0.01 M ionic strength determined by DLS are several times higher than the respective sizes determined by TEM, thus indicating an important particle aggregation in aqueous suspensions. Pb//nAp and Pb//SBO-Fe-nAp showed increased average hydrodynamic sizes than those of the corresponding Pb(II)-free particles (see Fig. 5). On the other hand, Pb//Fe-nAp and Fe-nAp show similar average size. All Pb(II)-containing particles show much higher size polydispersion than the respective Pb(II)-free particles.

3.3. On the Mechanisms of Pb(II)-Sorption

Fe-nAp, characterized by low crystalline hydroxyapatite domains and a surface containing iron phosphate and magnetite/maghemite phases shows multiple functionalities capable of supporting higher adsorption capacity than nAp. The diminution in the negative surface charge of Fe-nAp observed after Pb(II) adsorption strongly suggests the participation of surface reactions with Pb^{2+}/ $Pb(OH)^+$ ions present in the solutions at pH 6–7. Formation of Pb(II)-iron (hydr)oxide surface complexes, in coincidence with Pb(II) adsorption in geothite and ferrydrite[30] and on magnetite,[32] is suggested. Phosphohedyphane-like structures detected by XRD and supported by Ca(II) exchange with Pb(II) ions visualized in XPS experiments, also significantly contribute to the overall adsorption and supports the observed irreversibility of the process.

SBO-Fe-nAp isotherms show lower b but higher K_L values than Fe-nAp, thus indicating the availability of fewer and probably different binding sites for Pb(II) adsorption. As already pointed out, *vide supra*, the FTIR and XPS

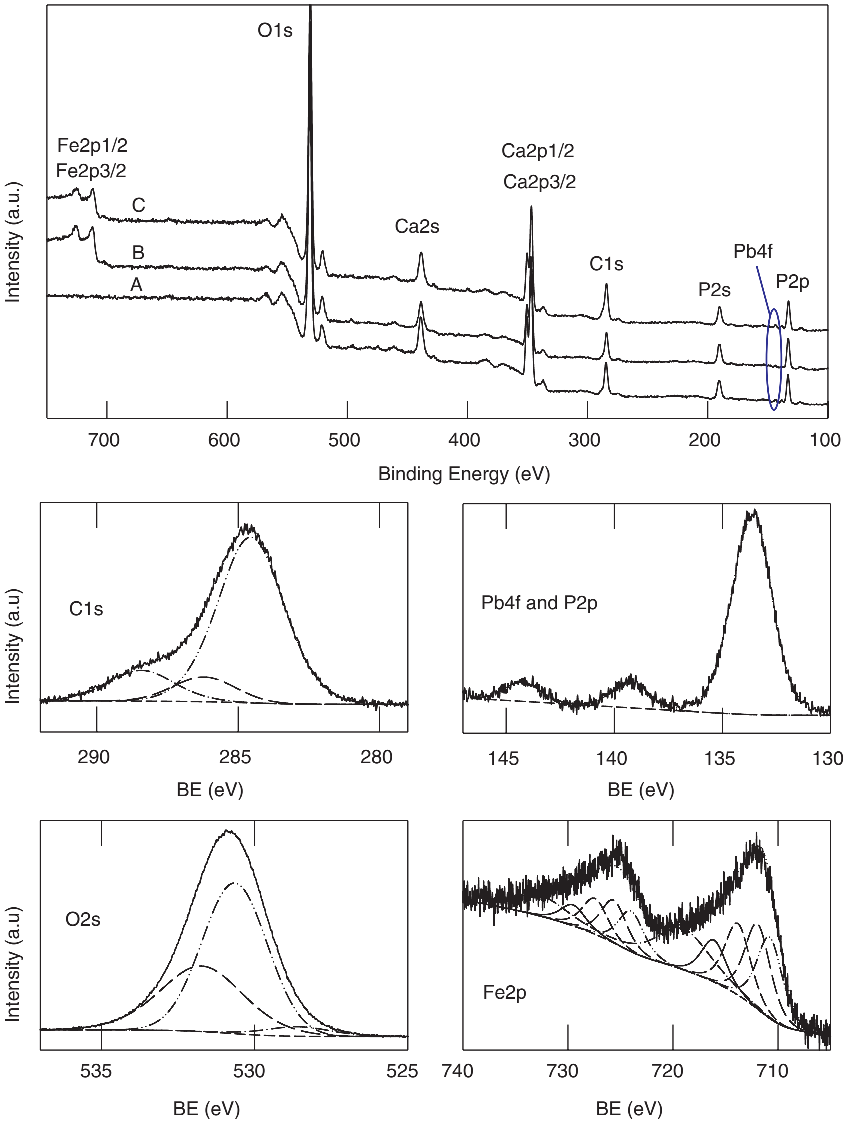

Figure 4. Top graph: XPS survey of Pb//nAp, Pb//Fe-nAp, and Pb//SBO-Fe-nAp (curves A, B, and C, respectively). Bottom graphs: C2s, P2p, Pb4f, O2s, and Fe2p signals (full lines) and contributing peaks (dashed lines) observed for Pb//SBO-Fe-nAp.

spectra of Pb//SBO-Fe-nAp strongly supports Pb(II) complexation with surface SBO hydroxyl and carboxyl groups. A rough estimation of the number of OH and COO^- binding sites present in the 5% weight of organic matter in SBO-Fe-Ap[10] may be obtained considering that SBO used in the present work contains *c.a.* 0.12 and 0.05 mole of COOH and phenolic groups per gram of carbon, respectively, and 38.25% of total organic C.[33] The estimated b

Table III. Electrophoretic mobilities in aqueous suspensions at pH 6.5–7 and 1–4 nm depth outer shell composition of the different samples as determined by XPS. The last digit error is given in parenthesis.

Sample	μ^a/ mS/cm	Composition^a	Sample	μ/mS/cm	Composition
nAp	+ 1.0 (2)	$Ca_{1.4}PO_{3.4}$	Pb//nAp	+ 1.3 (2)	$Ca_{1.4}PO_{4\cdot 2}Pb_{0.004}$
Fe-nAp	− 1.7 (1)	$Ca_{1.1}PO_{5.1}Fe_{0.155}$	Pb//Fe-nAp	− 0.8 (2)	$Ca_{0.9}PO_{3.9}Fe_{0.27}Pb_{0.009}$
SBO-Fe-nAp	− 1.8 (2)	$Ca_{1.25}PO_{4.6}Fe_{0.15}$	Pb//SBO-Fe-nAp	− 0.2 (2)	$Ca_{1.25}PO_{4.9}Fe_{0.25}Pb_{0.012}$

Note: ^{a}Data taken from Ref. [10].

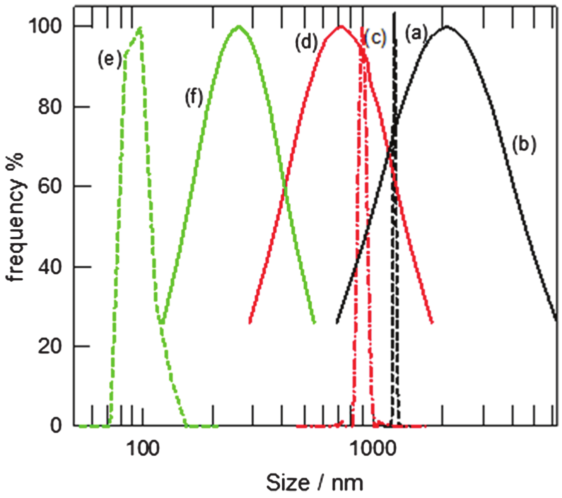

Figure 5. Hydrodynamic size distribution curves obtained by DLS of aqueous suspensions at pH 7 and 0.01 M ionic strength of (a) nAp (- - -), (b) Pb//nAp (—), (c) Fe-nAp (- - -), (d) Pb//Fe-nAp (—), (e) SBO-Fe-nAp (- - -), and (f) Pb//SBO-Fe-nAp (—).

value of 46 μmol m^{-2} is in line with the experimental value of 59 μmol m^{-2}, thus supporting a significant contribution of surface SBO to the Pb(II) adsorption capacity observed for SBO-patterned particles. The importance of organic matter as a sink for Pb(II) adsorption was also recognized in the literature for organic rich smelter-impacted soil.[34] Formation of pyromorphite- like structures observed in the DRX diffractogram indicates that these structures also partly contribute to the overall Pb(II) adsorption on Fe-nAp.

Since SBO may be regarded as a polymeric structure containing abundant carboxylate groups,[33] $Pb^{2+}/Pb(OH)^+$ ion coordination to SBO-carboxylate groups present in different particles may effectively lead to the formation of macrostructures[26] with low or no surface charge. These macrostructures may contribute to the increased particle agglomeration observed for SBO-Fe-nAp after Pb(II) adsorption.

The main changes introduced by Pb(II) adsorption on nAp herein evidenced are an important increase in the particles hydrodynamic size and a high polydispersion of apatite aggregates, while no important changes in the surface charge and surface Ca:P ratio, nor on the apatite cristalline structure, where observed. Formation of lead oxides is discarded from the XPS data though the same experiments show an increase in the O:P ratio upon Pb(II) adsorption. Literature reports[1,2,4,15,16] indicate that Pb(II) irreversible adsorption on hydroxyapatite crystals involves the dissolution of apatite followed by the precipitation of unstable hydroxypyromorphite-like structures with high Ca content. Despite the observed irreversibility of the adsorption process, no evidence was obtained from XRD and XPS data to unambigously support hydroxypyromorphite-like structures formation.

3.4. Simultaneous Adsorption of Cu(II) and Pb(II) Ions

Bi-metal Cu(II)-Pb(II) adsorption experiments allow to determine Pb(II) adsorption isotherms in the presence of an initial concentration of 6.4 ppm Cu(II), amount necessary to reach the Cu(II) maximum absorption on nAp and Fe-nAp single-metal experiments under similar experimental conditions. Figure 6 reports the obtained isotherms. For a better understanding on the ion adsorption competition, isotherms are expressed in mole ions per gram of substrate instead of the established units in gram ions per gram substrate.

Figure 6(a) shows that nAp adsorption isotherms of Pb(II) in bi- and single-metal experiments are coincident, while the adsorbed Cu(II) ions decrease upon increasing Pb(II) adsorption. The total number of adsorbed ions, n_T, reaches a value of *ca.* 0.6 mmol g^{-1} in the presence of high ion concentrations. The latter value is of the order of the maximum Pb(II) ion occupancy, $b_n = 0.67$ mmolg^{-1},

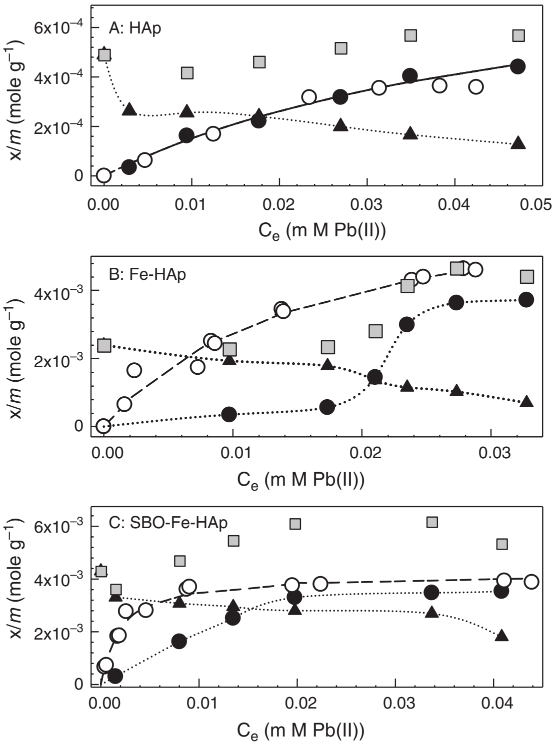

Figure 6. Pb(II) adsorption isotherms (●) and corresponding Cu(II) (▼) adsorption at 25 °C in bi-metal experiments on (A) nAp, (B) Fe-nAp, and (C) SBO-Fe-nAp. (■) stands for the total number of adsorbed ions (n_T). (○) Pb(II) adsorption isotherms in single metal experiments. Dashed lines stand for a fitting according to the Langmuir model and dotted lines stand as a guide to the eye.

estimated from the adsorption isotherms in single-metal experiments. These results seem to indicate that Cu(II) and Pb(II) ions share the same adsorption sites and that Pb(II) adsorption affinity for nAP is higher than that of Cu(II), in agreement with previous reports on synthetic hydroxyapatite.[3]

Bi-metal Cu(II)–Pb(II) adsorption experiments on Fe-nAp showed the competition between Cu(II) and Pb(II) ions depending on Pb(II) concentration (see Fig. 6(b)). Since higher n_T are observed for high Pb(II) concentrations, it suggests that Cu(II) and Pb(II) share the same adsorption sites, though the surface may accommodate more Pb(II) ions per surface area unit, and it shows somewhat higher adsorption affinity for Pb(II) ions than for Cu(II). Such behavior may be assigned to the smaller hydrated ionic radii of Pb(II) (4.01 Å) compared to that of Cu(II) (4.19 Å), in line with reported studies on Pb(II) and Cu(II) adsorption on soil adsorbents, also observing a favored formation of Pb(II) inner-sphere complexes with hydroxyl groups.[35]

On the other hand, bi-metal adsorption experiments performed with SBO-Fe-nAp showed a less significant competition between Cu(II) and Pb(II) ions (see Fig. 6 (c)). In this case, n_T is higher than the maximum adsorption capacity of Pb(II) ions, which clearly indicates that Cu(II) and Pb(II) may accommodate on different adsorption sites. In fact, Cu(II) adsorption capacity by SBO-patterned particles could not be assigned solely to SBO at the particles surface[10] whereas complexation with SBO functional groups is an important process for Pb(II) adsorption.

4. CONCLUSION

Hydroxyapatite-based nanoparticles are shown to be efficient adsorbants for the elimination of Pb(II) ions from aqueous solutions. Incorporation of 10% w/w Fe(II)/Fe(III) as iron oxides and phosphates increases hydroxyapatite Pb(II) cations adsorption capacity and turns the main apatite structures into paramagnetic supports[10] allowing their easy isolation from the water matrix with an applied magnetic field. Fe-containing hydroxyapatite particles with SBO at their surface also show an increased Pb(II) ion adsorption. The three hydroxyapatite-based powders herein investigated were able to support irreversible Pb(II) adsorption processes, an important condition for controlling Pb(II) bioavailability in the aqueous basins.

While hydroxyapatite nanoparticles are selective Pb(II) sorbents in solutions containing Pb(II) and Cu(II) ions, Fe-containing hydroxyapatite nanoparticles selectivity depends on the relative [Pb]/[Cu] ratio, and SBO-patterned Fe-containing hydroxyapatite is capable of adsorbing both ions with similar specificity. These observations clearly indicate that the surface chemistry of hydroxyapatite materials may be conveniently manipulated to obtain materials with adsorption selectivity to both Cu(II) and Pb(II) ions.

Acknowledgment: D. F. Mercado thanks Consejo Nacional de Investigaciones Científicas y Técnicas (CONICET, Argentina) for a graduate studentship. M. C. Gonzalez, P. Caregnato and A. Rubert are research members of CONICET. The work was performed partly with funds of the Ministero Italiano delle Politiche Agricole within the Agrienergia project and by the grant PICT 2012-2359 from Agencia Nacional de Promoción Científica y Tecnológica, Ministerio de Ciencia y Técnica, Argentina. Financial support for academic interchange by the European Union (IRSES-GA-2010-269128, EnvironBOS, and Horizon 2020 research and innovation program under the Marie Skłodowska - Curie grant, agreement No 645551, Mat4Treat) is acknowledged. The authors are grateful to the following private and/or public Italian institutions: (a) AceaPinerolese Spa in Pinerolo (TO) for supplying the SBO sourcing biowastes; (b) Studio Chiono and Associati in RivaroloCanavese (TO) for making available pilot equipment and services for the production of SBO.

References and Notes

1. E. Mavropoulos, A. M. Rossi, A. M. Costa, C. A. C. Perez, J. C. Moreira, and M. Saldanha, *Environ. Sci. Technol.* 36, 1625 **(2002)**.
2. V. Laperche, T. J. Logan, P. Gaddam, and S. J. Traina, *Environ. Sci. Technol.* 31, 2745 **(1997)**.
3. J. Chen, Y. Wang, D. Zhou, Y. Cui, S. Wang, and Y. Chen, *Environ. Prog. Sustain. Energy* 29, 233 **(2010)**.
4. D. Liao Dexiang, W. Zheng, X. Li, Q. Yang, X. Yue, L. Guo, and G. Zeng, *J. Hazard. Mater.* 177, 126 **(2010)**.
5. J. Cha, M. Cui, M. Jang, S. H. Cho, D. H. Moon, and J. Khim, *Environ. Geochem. Health* 33(SUPPL. 1), 81 **(2011)**.
6. Q. Y. Ma, S. J. Traina, T. J. Logan, and J. A. Ryan, *Environ. Sci. Technol.* 28, 1219 **(1994)**.
7. H. L. Clever and F. J. Johnston, *J. Phys. Chem. Ref. Data* 9, 751 **(1980)**.
8. J. Flis, M. Manecki, and T. Bajda, *Geochim. Cosmochim. Acta* 75, 1858 **(2011)**.
9. S. Jerdioui, L. L. Elansari, and B. Bouammali, *J. Mater. Envirom. Sci.* 6, 852 **(2015)**.
10. D. F. Mercado, G. Magnacca, M. Malandrino, A. Rubert, E. Montoneri, L. Celi, and A. B. Prevot, *ACS Appl. Mater. Interfaces* 6, 3937 **(2014)**.
11. S. Brundavanam, G. Eddy, J. Poinern, and D. Fawcett, *Am. J. Mater. Sci.* 5, 31 **(2015)**.
12. X. Cao, L. Q. Ma, D. R. Rhue, and C. S. Appel, *Environ. Pollut.* 131, 435 **(2004)**.
13. H. M. V. M. Soares and P. C. F. L. Conde, *Anal. Chim. Acta* 421, 103 **(2000)**.
14. S. T. Ramesh, N. Rameshbabu, R. Gandhimathi, M. Srikanth Kumar, and P. V. Nidheesh, *Appl. Water Sci.* 3, 105 **(2012)**.
15. S. P. Singh, L. Q. Ma, and M. J. Hendry, *J. Hazard. Mater.* 136, 654 **(2006)**.
16. T. L. Dowd, J. F. Rosen, L. Mints, and C. M. Gundberg, *Biochim. Biophys. Acta—Mol. Basis Dis.* 1535, 153 **(2001)**.
17. Li and Stanforth, *J. Colloid Interface Sci.* 230, 12 **(2000)**.
18. S. Nasrazadani, V. Paliwal, M. Du, R. F. Reidy, J. Stevens, and R. Theimer, *Corrosion* 64, 509 **(2008)**.
19. Y. I. N. Wang, Y. Xie, W. Li, Z. Wang, and D. E. Giammar, 44, 8950 **(2010)**.

20. L. Dong, Z. Zhu, Y. Qiu, and J. Zhao, *Chem. Eng. J.* 165, 827 (**2010**).

21. G. Pan and P. S. Liss, *J. Colloid Interface Sci.* 201, 77 (**1998**).

22. A. R. Kampf, I. M. Steele, and R. A. Jenkins, *Am. Mineral.* 91, 1909 (**2006**).

23. I. Rehman and W. Bonfield, *J. Mater. Sci. Mater. Med.* 8, 1 (**1997**).

24. J. Puy, J. Galceran, C. Huidobro, E. Companys, N. Samper, J. L. Garcés, and F. Mas, *Environ. Sci. Technol.* 42, 9289 (**2008**).

25. E. M. Logan, I. D. Pulford, G. T. Cook, and A. B. Mackenzie, *Eur. J. Soil Sci.* 48, 685 (**1997**).

26. M.-L. Hu, A. Morsali, and L. Aboutorabi, *Coord. Chem. Rev.* 255, 2821 (**2011**).

27. K. Nakamoto, Infrared and Raman Spectra of Inorganic and Coordination Compounds, 6th edn., Willey and Sons, New Jersey (**2009**), Vol. 156.

28. Nist, "NIST X-ray Photoelectron Spectroscopy Database, Version 4.1 (National Institute of Standards and Technology, Gaithersburg, 2012); http://srdata.nist.gov/xps/." (**2012**).

29. J. C. Sánchez-López, T. C. Rojas, J. P. Espinós, and A. Fernández, *Scr. Mater.* 44, 2331 (**2001**).

30. H. Abdel-Samad and P. R. Watson, *Appl. Surf. Sci.* 136, 46 (**1998**).

31. P. J. Cumpson and M. P. Seah, *Surf. Interface Anal.* 25, 430 (**1997**).

32. X. S. Wang, H. J. Lu, L. Zhu, F. Liu, and J. J. Ren, *Adsorpt. Sci. Technol.* 28, 407 (**2010**).

33. E. Montoneri, V. Boffa, P. Savarino, D. Perrone, M. Ghezzo, C. Montoneri, and R. Mendichi, *Waste Manag.* 31, 10 (**2011**).

34. G. Morin, J. D. Ostergren, F. Juillot, P. Ildefonse, G. Calas, and G. E. Brown, *Am. Mineral.* 84, 420 (**1999**).

35. F. Zhang, X. Ou, S. Chen, C. Ran, and X. Quan, *Front. Environ. Sci. Eng.* 6, 484 (**2012**).

Received: 29 April 2016. Accepted: 31 August 2016.